Astronomy & Astrophysics manuscript no. February 2, 2008
(DOI: will be inserted by hand later)

arXiv:astro-ph/0303100v1 4 Mar 2003

Bulge Microlensing Optical Depth from EROS 2 observations⋆

C. Afonso[1,5,11], J.N. Albert[2], C. Alard[3], J. Andersen[7], R. Ansari[2], É. Aubourg[1], P. Bareyre[1,5], F. Bauer[1], J.P. Beaulieu[6], G. Blanc[1], A. Bouquet[5], S. Char[8⋆⋆], X. Charlot[1], F. Couchot[2], C. Coutures[1], F. Derue[1,2⋆⋆⋆], R. Ferlet[6], P.Fouqué[10,12] J.F. Glicenstein[1], B. Goldman[1,5,11], A. Gould[5,9], D. Graff[9], M. Gros[1], J. Haissinski[2], C. Hamadache[1], J.C. Hamilton[5†], D. Hardin[1‡], J. de Kat[1], A. Kim[5§], T. Lasserre[1], L.LeGuillou[1], É. Lesquoy[1,6], C. Loup[6], C. Magneville[1], B. Mansoux[2], J.B. Marquette[6], É. Maurice[4], A. Maury[12], A. Milsztajn[1], M. Moniez[2], N. Palanque-Delabrouille[1], O. Perdereau[2], L. Prévot[4], N. Regnault[2], J. Rich[1], M. Spiro[1], P. Tisserand[1], A. Vidal-Madjar[6], L. Vigroux[1], S. Zylberajch[1]
The EROS collaboration

[1] CEA, DSM, DAPNIA, Centre d'Études de Saclay, 91191 Gif-sur-Yvette Cedex, France
[2] Laboratoire de l'Accélérateur Linéaire, IN2P3 CNRS, Université de Paris-Sud, 91405 Orsay Cedex, France
[3] DASGAL, INSU-CNRS, 77 avenue de l'Observatoire, 75014 Paris, France
[4] Observatoire de Marseille, 2 pl. Le Verrier, 13248 Marseille Cedex 04, France
[5] Collège de France, Physique Corpusculaire et Cosmologie, IN2P3 CNRS, 11 pl. M. Berthelot, 75231 Paris Cedex, France
[6] Institut d'Astrophysique de Paris, INSU CNRS, 98 bis Boulevard Arago, 75014 Paris, France
[7] Astronomical Observatory, Copenhagen University, Juliane Maries Vej 30, 2100 Copenhagen, Denmark
[8] Universidad de la Serena, Facultad de Ciencias, Departamento de Fisica, Casilla 554, La Serena, Chile
[9] Department of Astronomy, Ohio State University, Columbus, OH 43210, U.S.A.
[10] Observatoire de Paris, LESIA, 92195 Meudon Cedex, France
[11] Department of Astronomy, New Mexico State University, Las Cruces, NM 88003-8001, U.S.A.
[12] European Southern Observatory (ESO), Casilla 19001, Santiago 19, Chile

Received;accepted

Abstract. We present a measurement of the microlensing optical depth toward the Galactic bulge based on the analysis of 15 contiguous 1 deg^2 fields centered on $(l = 2.^\circ5, b = -4.^\circ0)$ and containing $N_* = 1.42 \times 10^6$ clump-giant stars (belonging to the extended clump area) monitored during almost three bulge seasons by EROS (Expérience de Recherche d'Objets Sombres). We find $\tau_{bulge} = 0.94 \pm 0.29 \times 10^{-6}$ averaged over all fields, based on 16 microlensing events with clump giants as sources. This value is substantially below several other determinations by the MACHO and OGLE groups and is more in agreement with what is expected from axisymmetric and non-axisymmetric bulge models.

Key words. Galaxy:bar - Galaxy:stellar contents - Galaxy:structure - Cosmology:gravitational lensing

1. Introduction

When microlensing surveys toward the Galactic bulge were first proposed by Paczyński (1991) and Griest (1991), it was expected that the optical depth to microlensing in the Baade Window $(l = 1^\circ, b = -3.^\circ9)$ due to ordinary disc lenses would be $\tau \sim 4 \times 10^{-7}$. In the presence of brown dwarfs in the disc with a total mass density equal to that of ordinary stars, the microlensing optical depth toward the bulge would rise to $\tau \sim 8 \times 10^{-7}$. The initial detections by OGLE reporting six microlensing events (Udalski et al. 1994a) seemed to indicate that the optical depth was higher than the predicted values, although no

Send offprint requests to: afonso@hep.saclay.cea.fr

⋆ Based on observations made with the MARLY telescope at the European Southern Observatory, La Silla, Chile.

⋆⋆ deceased

⋆⋆⋆ Presently at Centre de Physique des Particules de Marseille, IN2P3-CNRS, 163 Avenue de Luminy, case 907, 13288 Marseille Cedex 09, France

† Presently at ISN, IN2P3-CNRS-Université Joseph-Fourier, 53 Avenue des Martyrs, 38026 Grenoble Cedex, France

‡ Presently at LPNHE, IN2P3-CNRS-Université Paris VI et VII, 4 Place Jussieu, F-75252 Paris Cedex, France

§ Lawrence Berkeley National Laboratory, Berkeley, CA 94720, U.S.A.

estimate was published. Kiraga & Paczyński (1994) then realized that the contribution of lenses in the bulge had also to be considered and that the density of disc lenses had to be reevaluated. They concluded that the bulge itself would most likely dominate the event rate. Nevertheless, when OGLE obtained an optical depth in the Baade Window of $\tau = (3.3 \pm 1.2) \times 10^{-6}$ with a sample of 9 microlensing events (Udalski et al. 1994b) and MACHO made the first formal estimate $\tau_{bulge} = 3.9^{+1.8}_{-1.2} \times 10^{-6}$ (at $l = 2.^\circ55, b = -3.^\circ64$) based on 13 events with clump-giant sources (Alcock et al. 1997), the community found it quite surprising. In the same paper MACHO also derived $\tau = 2.4 \pm 0.5 \times 10^{-6}$, based on 41 events, including not only clump giants, but all sources. They argued, however, that the determination of the optical depth for fainter source stars is less straightforward than for bright ones due to blending problems in crowded fields, where a source star can be a blend of two or more stars. Hence the entire luminosity function has to be modeled to account for both resolved and unresolved sources.

Gould (1994) and Kuijken (1997) showed that the expected maximum optical depth generated by axisymmetric mass distributions of the Galaxy was surpassed by the observations. Indeed, attention was immediately focused on the possibility that the high microlensing rate represented yet another detection of a (non-axisymmetric) bar in the central regions of the Galaxy. At this time, a "bar consensus" was developing based on gas kinematics (Binney et al. 1991), infrared light measurements (Dwek et al. 1995), and star counts (Nikolaev & Weinberg 1997). However, even barred bulge models, with various values for the bar mass and the orientation to our line of sight, predict optical depths systematically lower than the observed values: Han & Gould (1995b) found $1.5 \times 10^{-6} < \tau_{bulge} < 2 \times 10^{-6}$ at the Baade Window for bulge-giant sources; Zhao et al. (1996) determined $\tau_{bulge} = 2.2 \times 10^{-6}$ for clump-giant sources at the MACHO field positions ($l = 2.^\circ.55, b = -3.^\circ64$); Zhao & Mao (1996) showed that several boxy and ellipsoidal-type bar models constrained by the COBE maps produce optical depths at the Baade Window 2σ lower than MACHO and OGLE measured values, even with a massive bar $M_{bar} = 2.8 \times 10^{10} \mathrm{M}_\odot$ and a small orientation angle $\theta < 20^\circ$ to the line of sight. Moreover, Binney, Bissantz & Gerhard (2000) recently showed that $\tau \sim 4 \times 10^{-6}$ cannot be produced by any plausible non-axisymmetric model of the Galaxy.

Up to the present there have been several other estimates of τ. Alcock et al. (2000) analyzed a subset of three years of MACHO data using difference imaging. This method increases the number of detected microlensing events. The mean optical depth (to the heterogeneous collection of bulge and disc sources in the MACHO fields) based on the 99 events found by this technique is estimated to be $\tau = 2.43^{+0.39}_{-0.38} \times 10^{-6}$ at ($l = 2.^\circ68, b = -3.^\circ35$). MACHO corrected this value to the true optical depth to bulge sources by assuming that 25% of the sources lay in the foreground and therefore did not contribute significantly to the observed microlensing events. They found the optical depth to be $\tau_{bulge} = 3.23^{+0.52}_{-0.50} \times 10^{-6}$. Another optical depth value is given by Popowski et al. (2000). Their analysis of 5 years of MACHO data revealed 52 microlensing events with clump-giant sources. The corresponding optical depth is $\tau_{bulge} = (2.0 \pm 0.4) \times 10^{-6}$ averaged over 77 fields centered at ($l = 3.^\circ9, b = -3.^\circ8$). A large fraction, perhaps a majority, of events detected toward the bulge have been found by OGLE II (Udalski et al. 2000, Wozniak et al. 2001) but so far these have not been used to estimate τ, as the OGLE II experimental detection efficiencies, necessary for the determination of microlensing optical depths, have not been made available yet.

In this paper we present the first estimate of the EROS 2 optical depth to microlensing toward the Galactic Center. The EROS 2 bulge survey, begun in July 1996, was specifically designed to find events with bright sources including the extended clump area (see Fig. 2)and other giants because, as discussed above, these can be interpreted unambiguously (Gould 1995b).

2. Data

The data were acquired at the EROS 2 team 1 m MARLY telescope at La Silla, Chile. The imaging was done simultaneously by two cameras, using a dichroic beam-splitter. Each camera is composed of a mosaic of eight 2K×2K LORAL CCDs, with a pixel size of $0.''6$ and a corresponding field of $0.^\circ7(\alpha) \times 1.^\circ4(\delta)$. One camera observes in the so-called EROS-blue filter and the other in the so-called EROS-red filter, these filters having been specifically designed to cover a broad passband to collect as many photons as possible. Thus, the EROS filters are non-standard: EROS-red (620-920 nm) is roughly equivalent to Cousins I, but larger, while EROS-blue (420-720 nm) is a band that overlaps Johnson/Cousins V and R. Details about the instrument can be found in Bauer et al. (1997). For information about the acquisition pipeline see Palanque-Delabrouille (1997).

Although the total sky area covered by the EROS bulge survey is $82\,\mathrm{deg}^2$, the observations reported here concern only 15 of these fields, monitored between mid-July 1996 and 31 May 1999. Fig.1 shows the location of the 82 fields in the galactic plane (l, b). We also indicate the fields classified as high-priority (solid line), with the largest number of red clump giants, which we attempt to observe every other night. The lower priority fields (dashed line) are monitored only if there is still enough time left after the high-priority sequence, taking into account the compromise between the bulge survey and other EROS targets: Spiral Arms (Derue et al. 2001), LMC (Lasserre et al. 2000), SMC (Afonso et al. 1999), proper motion survey (Goldman et al. 2002), supernova search (Hardin et al. 2000). The 15 fields whose analysis is presented here are marked in bold. The corresponding data set contains 2.3×10^6 light curves, of which 1.4×10^6 are bulge clump giants of the extended clump area (see Fig. 2). As we mentioned above, our bulge program was specifi-

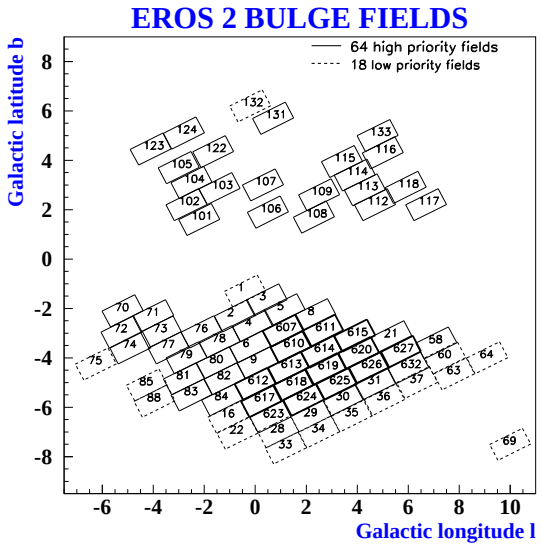

Fig. 1: Galactic plane map of the EROS 2 bulge fields. A total of 82 fields are monitored. The high priority fields are supposed to be observed at least every other night (solid lines). The lower priority fields (dashed lines) are only monitored if some observation time is still available after the high prioriy sequence. The analysis and the results reported in this paper concern 15 deg^2 (bold lines).

cally designed to select events with bright stars as sources to avoid blending problems. Since one of the red CCDs was not functioning well during a large fraction of the observation period, it was not included in our analysis, since we require two colours.

3. Event Selection

The image photometry was performed with software specifically designed for crowded fields, PEIDA (Photométrie et Étude d'Images Destinées à l'Astrophysique) (Ansari 1996). After the production of the light curves and removal of defective data points due to images with a specific problem (bad atmospheric conditions, temporary instrumental deficiencies), several cuts were applied to the data set. The selection criteria explained in detail below are based on the characteristics of microlensing events light curves, which follow the Paczyński (1986) function

$$F(t) = F_{\rm s} A[u(t)] \quad (1)$$

$$\text{where} \quad A(u) = \frac{u^2+2}{u\sqrt{u^2+4}} \quad (2)$$

$$\text{and} \quad u^2(t) = u_0^2 + \frac{(t-t_0)^2}{t_{\rm E}^2}\,. \quad (3)$$

These equations contain 5 parameters (which are obtained for each star by fitting the Paczyński profile to the corresponding light curve): two baseline fluxes ($F_{\rm s}$) of the source star in the red and blue EROS filters, $F_{\rm R_{EROS}}$ and $F_{\rm B_{EROS}}$, the date of maximum amplification t_0, the impact parameter $u_0 = u(t_0)$ (i.e. the minimum lens-source separation projected in the lens plane, normalized by the Einstein ring radius $R_{\rm E}$) and finally, the microlensing event duration, i.e. the Einstein ring radius crossing time $t_{\rm E} = R_{\rm E}/v_{\rm t}$. The time scale $t_{\rm E}$ contains a 3-fold degeneracy between the transverse velocity $v_{\rm t}$ of the lens, its mass M, and its distance from the observer $D_{\rm OL}$. The $t_{\rm E}$ dependence on the mass and the distance comes through $R_{\rm E}^2 = 4GMD_{\rm LS}D_{\rm OL}/c^2D_{\rm OS}$, where $D_{\rm OS}$ is the distance between the observer and the source and $D_{\rm LS}$ the distance between the lens and the source.

The main characteristics of an amplified light curve of a source star during gravitational microlensing are a symmetric shape in time, with an increasing light intensity as the foreground lens approaches the line of sight to the background source star, and then decreases as the lens moves away (assuming a constant transverse velocity v_t of the lens). When blending is neglected, the amplification $A[u(t)]$ is the same in the two observing bands (the imaging being done simultaneously in both bands) and therefore achromatic, since microlensing is a purely geometrical phenomenon and should thus not depend on the observing wavelength. When the reconstructed star is a blend of two or more stars, the observed baseline flux $F_{\rm s} = F_1 + F_2$ is the sum of the flux F_1 of the main component of star and the flux F_2 due to unresolved background stars. Assuming that the main component is amplified by a factor $A(t)$, the observed flux during the amplification is given by $F(t) = F_1A(t) + F_2 = F_{\rm s}A_{\rm obs}(t) = ACF_{\rm s}A(t) + (1-C)F_{\rm s}$ where $C = (A_{\rm obs}(t)-1)/(A(t)-1)$ is the blending coefficient and $A_{\rm obs}(t)$ is the observed amplification.

Finally, another main characteristic is that the amplification peak should be unique for a given source star, as the probablitity of a star to be lensed is extremely low, of the order of one per 10^6 stars. If two or more variations occur, the source star is more likely to be variable. Thus, several of our cuts concern the rejection of variable stars.

Hereafter we describe the selection criteria, which are similar to those used in the other EROS microlensing programs.

1. **Rejecting stable stars**

   (a) The main fluctuations in both the red and blue light curves should be positive[1], and should overlap in time by at least 10%.

   (b) To select light curves with a significant main fluctuation we use the discriminant LP^2, to which no true statistical meaning is assigned. It is rather

[1] A positive (negative) fluctuation is defined as a set of consecutive points that deviate by at least 1σ above (below) the baseline flux.

[2] The statistical significance of a fluctuation containing N points is given by $LP = -\sum_{i=1}^{i=N} \log\left(\frac{1}{2}\,\mathrm{Erfc}\left(\frac{x_i}{\sqrt{2}}\right)\right)$, with each point i deviating at time t_i by x_i (in units of σ_i, the error for the i-th flux measurement).

used in an empirical and relative manner, in the sense that the light curves with higher LP values than other light curves have a more significant variation. Thus we require that the main fluctuation in both colours is significant: $LP(\text{main fluct.}) > 40$.

2. **Eliminating variable stars**

(a) To reject the scattered light curves of short period variable stars, which vary on time scales shorter than the average time sampling of our fields, the following requirement is made: the distribution of the difference, in units of $\sigma_{\rm i}$ (the error for the i-th flux measurement) , between each flux $F(t_{\rm i})$ and the linear interpolation of the two adjacent neighbors $F(t_{\rm i-1})$ and $F(t_{\rm i+1})$, should have an RMS lower than 2.5.

$\sigma_{int} < 2.5$,

(b) Longer period variable stars display variations in both red and blue bands. They are likely to show such correlated variations outside the principal fluctuation. Such correlations are searched for using the Fisher variable (FV) which is a function of the correlation coefficient ρ between the red and blue fluxes. This variable allows one to distinguish, with a better resolution, between correlation values very close to each other and thus to tune more precisely the cut. We require

$$FV(\rho) = 0.5 \times \sqrt{N-3} \times \ln\left(\frac{1+\rho}{1-\rho}\right) < 13 \ ,$$

where N is the number of pairs of simultaneous measurements in the red and blue bands, belonging to the unamplified part of the light curve. The exclusion of the principal fluctuation (plus a security time margin) guarantees the survival of the microlensing candidates, which as expected exhibit a strong correlation within the amplification peak.

(c) The following rejection criterion is similar to 2(a) and 2(b), eliminating the variable stars that passed these cuts. We keep only the light curves that have a stable baseline outside the principal fluctuation in both bands

$$\chi^2(baseline) = \frac{\chi^2_{\rm ml}(baseline)}{d.o.f.(baseline)} < 5 \ ,$$

where $\chi^2_{ml}(baseline)$ and $d.o.f.(baseline)$ are respectively the chi square of the microlensing fit (carried out separately in each band) and the number of degrees of freedom of the fit, both values concerning the unamplified part of the light curve.

3. **Selecting high S/N events**

(a) To select events with a high signal-to-noise ratio (S/N) a cut is applied to a semi-empirical estimator, whose value will increase as a microlensing fit (ml) improves over a constant-flux fit (cst)

$$\Delta\chi^2 = \frac{\chi^2_{\rm cst} - \chi^2_{\rm ml}}{\chi^2_{\rm ml}/d.o.f.} \frac{1}{\sqrt{2d.o.f.(peak)}} \ ,$$

where $d.o.f.$ is the number of degrees of freedom of the fit over the entire light curve and $d.o.f.(peak)$ refers to the number of degrees of freedom of the fit within the amplification peak. For the fits we use simultaneously the data points of both red and blue light curves. We require $\Delta\chi^2 > 70$.

(b) Candidates with low fitted maximum amplifications $A(u_0)$, may be due to statistical fluctuations or systematic photometry biases, or may be impossible to distinguish from these when the photometric precision of the stars (which for clump giants is of the order of 2-3%) does not allow it. To remove these candidates from the remaining set, we demand for each star that its maximum amplification be greater than 5 times the photometric precision of the star (calculated from the unamplified part of the light curve). For a 2-3% photometric precision, this cut allows the detection of maximum amplifications as low as 10%.

4. **Date of maximum amplification and time span allowing to validate a candidate**

(a) Although the above criteria select candidates that *a priori* are microlensing events, some exhibit their date of maximum amplification t_0 just before or after the observation period. The confirmation of a candidate for which we have only the decreasing or increasing part of the amplification peak on the light curve is extremely difficult, if not impossible. Thus, we require that the fitted date of maximum amplification t_0 is within the observation period

$$T_{\rm first} - \frac{t_{\rm E}}{3} < t_0 < T_{\rm last} + \frac{t_{\rm E}}{3} \ ,$$

where $t_{\rm E}$ is the event time scale, T_{first} is the first day of the observations and T_{last} the last one. A margin is allowed ($t_E/3$) due to the uncertainty of the fitted t_0 value.

(b) As for the previous cut, it is also difficult to confirm candidates with time scales $t_{\rm E}$ too long compared to the observation period ($T_{\rm obs} \sim 3$ years), even if the date of maximum amplification is contained in the light curve. We demand that the observation period be at least 3 times greater than the Einstein ring radius crossing time $t_{\rm E}$, so that the starting or ending points of the amplification are visible on the light curves. The candidates removed by this cut from the final set (with $t_{\rm E} > 400$ days), are kept on a list for regular follow-up and checking, as they could be due to black holes or neutron stars.

To be chosen as a candidate, the light curve must satisfy each one of the above listed criteria. These are tuned

by applying the same selection criteria to the data and to a set of simulated microlensing events (generated on top of the real light curves, see §5). One tries to eliminate a maximum of false candidates, while keeping the greatest possible number of simulated events. In order to detect also non-standard microlensing events (source size effect, caustic crossing), the selection criteria have been tuned sufficiently loosely.

4. EROS 2 bulge microlensing candidates

The selection criteria presented in the previous section yield a total of 33 microlensing candidates, of which 25 have clump-giant sources (belonging to the extended clump area). Fig. 2 shows the location of the source stars for the 33 microlensing candidates in an instrumental colour-magnitude diagram (CMD). This diagram was obtained by splitting up the EROS 0.7×1.4 deg^2 field into 32 0.17×0.17 deg^2 sub-fields, finding the center of the clump of each of the sub-fields and then aligning them independently to an arbitrary common position on an instrumental CMD, which was chosen to be the EROS field centered on the Baade Window. To define $R_{\rm EROS}$ and $B_{\rm EROS}$ magnitudes, stars in the OGLE Baade Window catalog (with field coordinates $\alpha(J2000) = 18^h03^m37, \delta(J2000) = -30°05'00''$) (Paczyński 1991) were matched with EROS stars

$$R_{\rm Eros} = 26.95 - 2.5 \times \log(F_{\rm R_{EROS}}) \quad (4)$$

$$B_{\rm Eros} = 27.86 - 2.5 \times \log(F_{\rm B_{EROS}}) \, . \quad (5)$$

where $F_{\rm R_{EROS}}$ and $F_{\rm B_{EROS}}$ are the red and blue fluxes (in ADU/120 s) of the center of the clump in the EROS sub-field corresponding to the Baade Window. The source stars of the microlensing candidates believed to be clump giants of the extended clump area are marked with solid circles, and sources other than clump giants are depicted with crosses. The markers surrounded by open circles refer to microlensing candidates with a maximum amplification $A_0 > 1.34$, i.e. an impact parameter $u_0 < 1$. The hatched area indicates the variation from field to field of the CMD adopted apparent magnitude cuts. Indeed, as we already mentioned in §1, the purpose of the EROS bulge program was to find events with bright sources so as to avoid uncertainties due to blending. The selection of these sources was made by determining the center of the clump in the CMD of each sub-field with a special search algorithm, and rejecting all the stars below the lower limit of the clump minus 0.5 magnitude. The lower limit of the clump is defined as being 1.5σ away from the mean of a Gaussian fitted along the magnitude axis of the CMD. Finally, the dashed lines delimit the extended clump area.

To obtain a reliable value for the bulge optical depth to microlensing, the least affected by systematic errors due to blending, we decided to consider only events with clump-giant sources (of the extended clump area), and to make a final cut requiring $u_0 < 1$, because it is difficult to totally

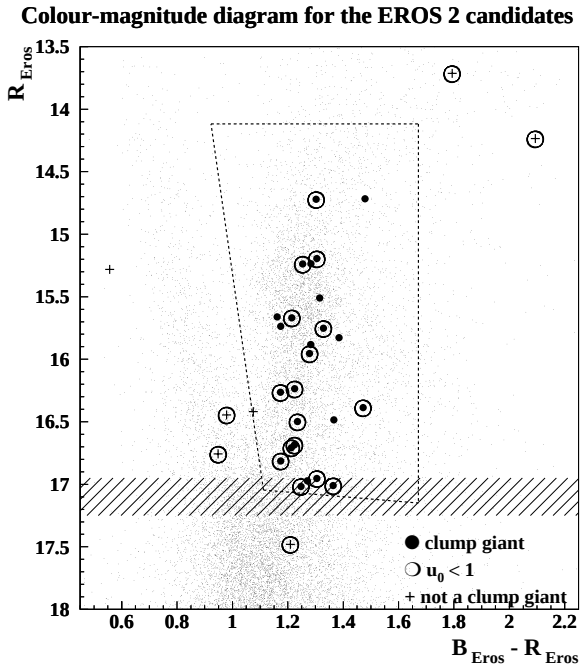

Fig. 2: Colour-magnitude diagram (CMD) for the source stars of the EROS 2 microlensing candidates superimposed (after alignment) on the CMD of the stars of the EROS sub-field centered on the Baade Window. Clump-giant sources (of the extended clump area) of the microlensing candidates are indicated with solid circles. Sources other than clump giants are marked with crosses. The empty circles surrounding the markers refer to microlensing candidates with a maximum amplification $A_0 > 1.34$. The magnitude cut in the CMD for the selection of bright reference source stars varies from field to field. This variation is indicated by the hatched area. Finally, the dashed lines surround the extended clump area containing the stars used for the optical depth calculation.

rule out other forms of stellar variability for lower amplification events. This selection yielded 16 events. In 2 cases, we found that the microlensing fit was improved by adding two additional parameters for parallax (Gould 1992), $\pi_{\rm E}$, the amplitude of the displacement in the Einstein ring due to the Earth's orbital motion, and ϕ, the phase of that displacement (see Table 3, Fig. 14 and Fig. 15). We also searched for blending effects on the selected sample of 16 candidates. Two light curves seem to be affected, showing a significant improvement of the microlensing fit when blending is taken into account, particularly for candidate #9 (see Table 3, Fig. 12 and Fig. 13).

Fig. 10 to 15 show the light curves for the 16 events. In Table 3 we present the characteristics of the 16 microlensing candidates with clump-giant sources (of the extended clump area) and $u_0 < 1$. The mean and standard deviation of the time scales distribution (see Fig. 3) for these events are

$$\langle t_{\rm E} \rangle = 33.3 \text{ days} \quad (6)$$

$$\sigma(t_{\rm E}) \ = \ 39.6 \text{ days} \ . \qquad (7)$$

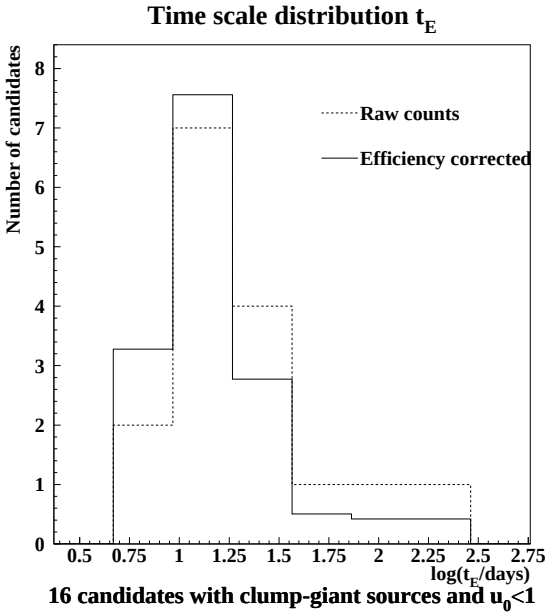

Fig. 3: Time scales distribution of the 16 microlensing candidates with clump-giant sources (of the extended clump area) and $u_0 < 1$ ($A_0 > 1.34$). The dashed line shows the raw data, while the solid curve is corrected for the detection efficiency. For the sake of comparison, the distribution of the corrected data was scaled so that the two histograms have the same area.

In order to check whether the experimental distribution of the observed impact parameters are drawn from the same distribution as the one expected for microlensing events, we use a Kolmogorov-Smirnov test. The theoretical cumulative distributions are calculated by selecting the Monte Carlo (MC) simulated events (generated randomly, see §5) with the same order of time scales as the observed ones and that were chosen by our analysis cuts. This method takes implicitly into account the detection efficiency, which will be presented in the next section. Fig. 4 shows the cumulative distribution of the impact parameters for the 16 candidates with clump-giant sources (of the extended clump area) and $u_0 < 1$. The dotted line refers to the expected $u_{0\rm MC}$ distribution for microlensing. The Kolmogorov-Smirnov probability $P_{\rm KS}$ indicates the significance of the similarity of two distributions at distance $D_{\rm max}$ from each other. We obtain $D_{\rm max} = 0.23$ which corresponds to $P_{\rm KS} = 34\%$, which shows a good agreement between the measured and expected distributions.

5. Detection efficiency

To determine the optical depth (see Eq. 9), we first evaluate the detection efficiency for each field as a function of time scale by using Monte Carlo simulated light curves.

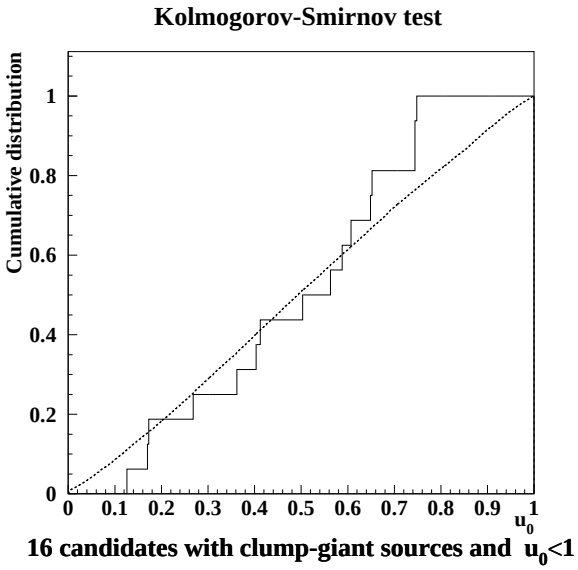

Fig. 4: Kolmogorov-Smirnov test for the impact parameter of the 16 candidates with clump-giant sources (of the extended clump area) and $u_0 < 1$. The maximal distance between the experimental cumulative distribution of u_0 (solid line) and the expected one (dashed line) is $D_{\rm max}$=0.23. This yields a Kolmogorov-Smirnov probability $P_{KS}(D_{\rm max})$=34%.

We superimpose artificial microlensing events, with randomly generated parameters (impact parameter, date of maximum amplification and time scale), on each of the real monitored light curves, and find the fraction that are recovered by our detection algorithm. Thus, the detection efficiency is given by

$$\epsilon(t_{\rm EMC} \ \in \ bin\ i) = \frac{N_{\rm DE}(t_{\rm E} \ \in \ bin\ i)}{N_{{\rm GE},u_{0\rm MC}<1}(t_{\rm EMC} \ \in \ bin\ i)} \qquad (8)$$

where $t_{\rm EMC}$ is the generated time scale, $N_{\rm DE}$ is the number of simulated events detected by our analysis, $t_{\rm E}$ is the time scale obtained by the microlensing fit, and $N_{{\rm GE},u_{0\rm MC}<1}$ is the number of generated events with an impact parameter $u_{0\rm MC} < 1$.

The microlensing parameters of the simulated events are drawn uniformly: the impact parameter $u_{0\rm MC}$ in the interval [0,2] and the date of maximum amplification $t_{0\rm MC}$ in the observation period, with a margin of 180 days before and after respectively the first and last day of the observations $[T_{\rm first} - 180, T_{\rm last} + 180]$. The time period for the detection efficiency determination, equal to 1418 days, corresponds to the observation period (1058 days) extended by a 180 days margin on both sides, in order to check whether we are sensitive to microlensing events with maximum magnification occurring just before or after the actual observation period. Finally the Einstein ring radius crossing time $t_{\rm EMC}$ is drawn uniformly from a $log(t_{\rm EMC})$ distribution (to enhance the efficiency precision at small time scales) over the interval [1,180] days. Efficiencies were

calculated only until $t_{\rm E} = 180$ days because there were no events detected longer than 145 days. Fig. 5 shows these efficiencies averaged over two sub-groups of 10 fields (solid line) and 5 fields (dashed line), as well as the global detection efficiency which is the average over all 15 fields (bold line). These sub-groups refer to the most and least densely sampled light curves, with ~ 350 data points and ~ 180 points respectively within the observation period, which is the same for all fields (1058 days). For the high signal to noise events used in this paper, the efficiency is affected mostly by time gaps in the data. For example, for long events with $t_{\rm E} \sim 100$ days, the 60% efficiency reflects the non-observability of the galactic center during the southern summer. Shorter time scale events are affected by periods of bad weather and instrumental failures.

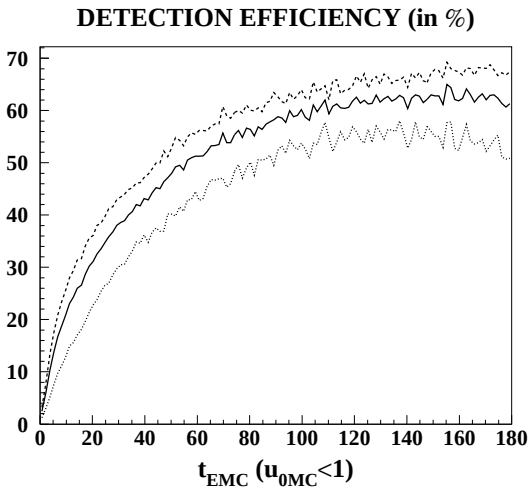

Fig. 5: Detection efficiency as a function of the event time scale (in days) averaged over all 15 fields (solid line) and two sub-groups of 10 fields (dashed line) and 5 fields (dotted line), with different time sampling: $\sim$ 350 and $\sim$ 180 data points respectively.

6. Optical Depth

The microlensing optical depth can be defined as the probability that a given star, at a given time t, is magnified by at least 1.34, i.e. with an impact parameter $u(t) < 1$. The optical depth is then given by

$$\tau = \frac{\pi}{2 N_\star T_{\rm obs}} \sum_{i=1}^{N_{\rm ev}} \frac{t_{\rm E,i}}{\epsilon(t_{\rm E,i})} \ , \qquad (9)$$

where $N_\star$ is the number of monitored stars, $T_{\rm obs}$ is the observation period, $t_{\rm E,i}$ is the measured Einstein ring radius crossing time of the ith candidate and $\epsilon(t_{\rm E,i})$ is the corresponding global detection efficiency (see Fig.5). Note that the above expression for τ only applies to objects whose mass and velocity cause events in the time scale range with significant efficiency. There could be more optical depth from events outside this range.

In Table 1 we summarize the time scales of the 16 microlensing candidates with clump-giant sources (of the extended clump area) and $u_0 < 1$, and the detection efficiencies for each measured $t_{\rm E}$.

Candidate	Name	$t_{\rm E}$ (days)	$\epsilon(t_{\rm E})$ (in %)
#1	EROS-BLG-16	4.7	14.2
#2	EROS-BLG-35	8.5	21.0
#3	EROS-BLG-3	9.3	22.3
#4	EROS-BLG-28	10.0	23.4
#5	EROS-BLG-2	10.4	23.8
#6	EROS-BLG-32	10.8	24.7
#7	EROS-BLG-13	13.1	27.0
#8	EROS-BLG-33	15.7	29.1
#9	EROS-BLG-31	18.3	32.0
#10	EROS-BLG-23	20.6	34.0
#11	EROS-BLG-11	30.3	40.3
#12	EROS-BLG-5	35.6	43.0
#13	EROS-BLG-18	35.8	43.0
#14	EROS-BLG-4	56.2	54.7
#15	EROS-BLG-29	108.3	63.4
#16	EROS-BLG-12	145.6	62.8

Table 1: The Einstein ring radius crossing time $t_{\rm E}$ and corresponding detection efficiency are shown for the 16 microlensing candidates with clump-giant sources (of the extended clump area) and $u_0 < 1$.

Fig. 3 shows the time scale distribution of the raw counts (dashed line) and corrected for efficiency (solid line), a rescaling factor having been applied so that the histograms have the same area. For the derivation of the optical depth we replace the parameters of Eq. (9) by the corresponding values: $N_\star = 1.42 \times 10^6$, equal to the number of clump giants (of the extended clump area), $T_{\rm obs} = 1418$ days which corresponds to the actual time period of the generation of simulated events (for the detection efficiencies determination, see §5), and finally the time scales and efficiencies found in Table 1. In the case of the 2 events affected by parallax, we considered the time scale obtained when taking into account this effect, but used the efficiencies for the time scales $t_{\rm E}$ determined from a simple microlensing fit without parallax, as initially found by our analysis. Regarding the events with blending, we used the time scale uncorrected for this effect, otherwise we would have had to estimate the number of blended unseen stars to add it to our optical depth equation. We have checked that the measured optical depth depends very little on these assumptions. Moreover, as we will justify below in a study to quantify the effect of blending on bright stars, these are on average unaffected. We obtain a bulge microlensing optical depth of

$$\tau = 0.94^{+0.29}_{-0.30} \times 10^{-6} \ \ at \ \ (l, b) = (2.^\circ 5, -4.^\circ 0) \ . \qquad (10)$$

Note that the optical depth, and the associated errors, are valid only for objects within the range of detection

~ 2 days $< t_E <$ 180 days. The (l, b) position is an average of positions of the clump giants (of the extended clump area) in the 15 fields. The uncertainties are statistical, estimated using the same technique as in Alcock et al. (2000). To do so, a significant number of experiments were simulated. For each experiment we generated the number n of "observed" microlensing events, according to Poisson statistics with a mean of $\mu = 16$, equal to the number of actually observed candidates. To each of the n events, one of the 16 measured time scale was assigned randomly (being uniformly drawn), thus obtaining an optical depth estimate for each virtual experiment. The uncertainties are then given by the $\pm 1\sigma$ values from the average of the simulated optical depth distribution (see Fig. 6). The 2σ can be calculated in the same way, yielding $\tau = 0.94^{+0.68}_{-0.46} \times 10^{-6}$.

The errors can also be estimated analytically (Han & Gould 1995b)

$$\sigma(\tau) = \tau \frac{\sqrt{< t_{\rm E}^2/\epsilon^2 >}}{< t_{\rm E}/\epsilon >} \frac{1}{\sqrt{N_{\rm ev}}} = 0.29 \times 10^{-6} \ , \qquad (11)$$

in very good agreement with the uncertainties given in Eq. (10).

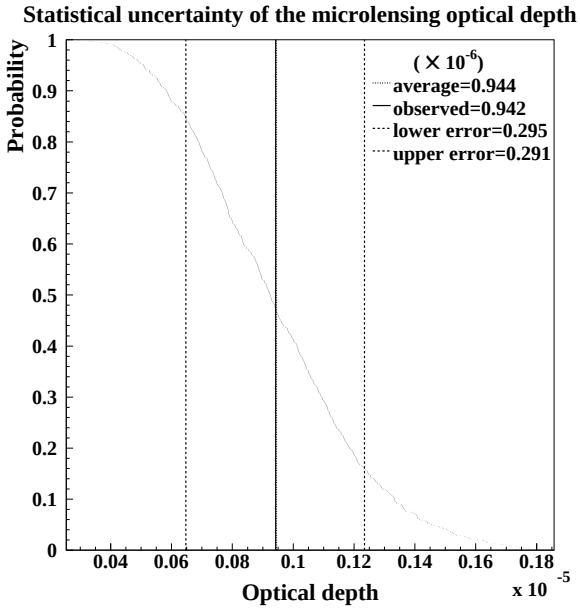

Fig. 6: The cumulative distribution of the statistical microlensing optical depth drawn from a significant number of virtual experiments for our sample of 16 microlensing candidates. The optical depth uncertainties are then given by the $\pm 1\sigma$ confidence limits (dashed lines).

The contribution of each of the 16 candidates to the measured optical depth is shown in Fig. 7, where the area of the cercles is proportional to the individual optical depth due to each event $\tau_i = \pi/(2N_{\star,\rm j}T_{\rm obs})t_{\rm E,i}/\epsilon(t_{\rm E,i})$, $N_{\star,\rm j}$ being the number of stars in field j, with the shortest event lasting ~ 5 days and the longest ~ 146 days. We also show the measured optical depth in each field.

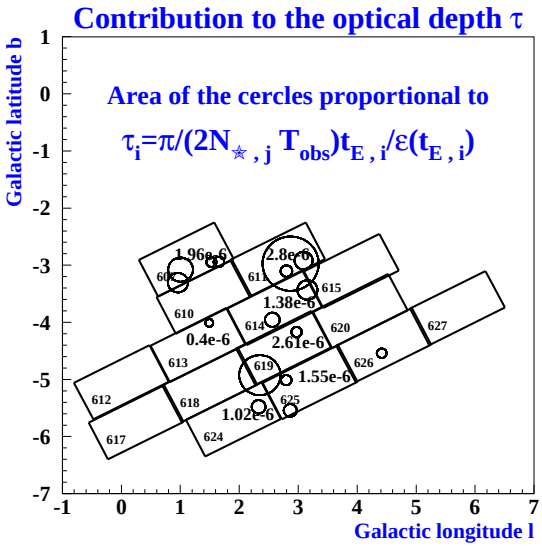

Fig. 7: The contribution of the 16 candidates to the observed optical depth. The area of the circles is proportional to the optical depth due to each microlensing candidate. The measured optical depth in each field is also shown, as well as the number of the EROS fields.

7. Effect of blending on the measured optical depth

In order to check that the measured optical depth given by microlensing events with clump-giant sources is not significantly affected by blending, we created a set of artificial images with simulated microlensing events, and calculated the optical depth from the candidates detected by our selection pipeline on the simulated light curves. Two types of synthetic images, corresponding to the two EROS passbands (see §2) and with a size of 512×512 pixels, were generated from a catalog derived from the Holtzman et al. (1998) luminosity function in the Baade Window. The catalog contained 365,000 stars which were placed randomly over the 512×512 pixels area. The faintest catalog star was 8 magnitudes dimmer than the faintest reconstructed star considered in this paper.

On an arbitrarily selected synthetic reference image, 20% (73,000) of the total number of artificial stars were chosen to be microlensed. We then generated in each color a sequence of 3,600 images equally spaced in time, the unit of time being 1 image. On each ensemble of 2×20 images (blue and red filters), about 400 microlensing events were generated. To avoid photometric interference between simulated events, only stars at least 20 pixels away from each other and with similar magnitudes were lensed. The microlensing events were generated with impact parameter u_0 randomly drawn between 0 and 1.5, date of maximum amplification t_0 equal to the center of the ensemble with a margin of 0.5 images, and time scale $t_{\rm E} = 5$ images. For the microlensing fit we used the ensemble containing the

fluctuation, plus an additional 20 images generated with no events in order to determine the baseline.

Roughly 10,000 stars of the total number of artificial stars were reconstructed by our software on each synthetic image, an example of which is shown in Fig. 8. To define a sample of bright stars a magnitude cut was performed on the CMD of the synthetic reference image (see Fig. 9). A total of 2270 stars were selected, corresponding closely to the mean density of bright stars reconstructed on real EROS images. The analysis pipeline was then applied to the simulated light curves of this sample of reconstructed bright stars.

A total of 411 generated microlensing events were found with an impact parameter $u_0 < 1$ and an average of reconstructed parameters $< t_{\rm E} >= 3.55$ images and $< u_0 >= 0.56$. From these events, 255 were due to the main star, i.e. the brightest catalog input star in the two pixels around the reconstructed star, with recovered $< t_{\rm E} >= 4.67$ images and $< u_0 >= 0.49$. The remaining 156 events are due to the fainter, blended, component of the reconstructed star. The average of the recovered time scales for these blended events is $< t_{\rm E} >= 1.72$ images, clearly underestimated, and $< u_0 >= 0.66$, overestimated.

In the absence of blending and with perfect photometric resolution, the number of simulated microlensing events one would expect to recover is $2270 \times 0.2/1.5 = 302$, where 2270 is the number of reconstructed bright stars selected by the magnitude cut in the CMD and 0.2 is the fraction of catalog stars microlensed with impact parameters less than 1.5. The optical depth being proportional to the product of the number of events passing the microlensing selection criteria and their mean $t_{\rm E}$, the ratio R of the recovered optical depth with the generated one yields

$$R = \frac{411}{302}\frac{3.55}{5.0} = 0.97 \qquad (12)$$

where 411 is the number of simulated microlensing events found by our analysis pipeline, the value 3.55 is the average of the recovered time scales, 302 is the number of simulated microlensing events one would expect to recover and 5.0 the average of the input time scales. The error of the ratio R is estimated to be 10%. This figure is based on the statistical error and from small differences in results obtained by varying within reason the form of the PSF used to generate synthetic images. The recovery of 97% of the generated optical depth is a reassuring result. Thus, our conclusion is that we can neglect blending effects on the optical depth inferred from microlensing events with bright source stars.

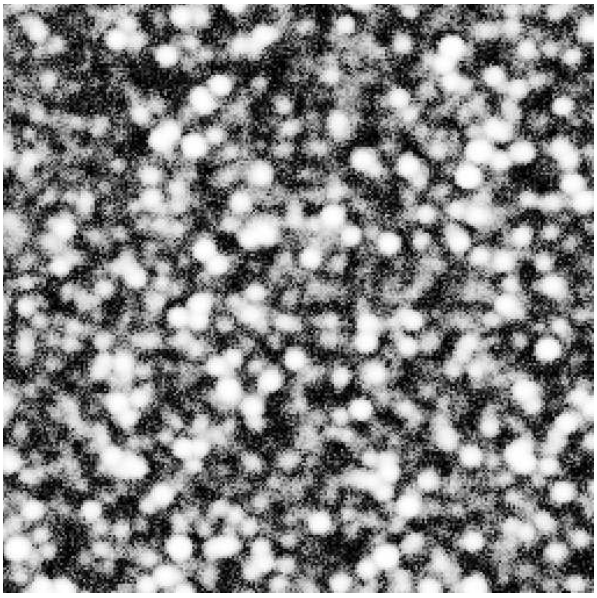

Fig. 8: Example of a synthetic image as described in §7 (256×256 pixels are shown).

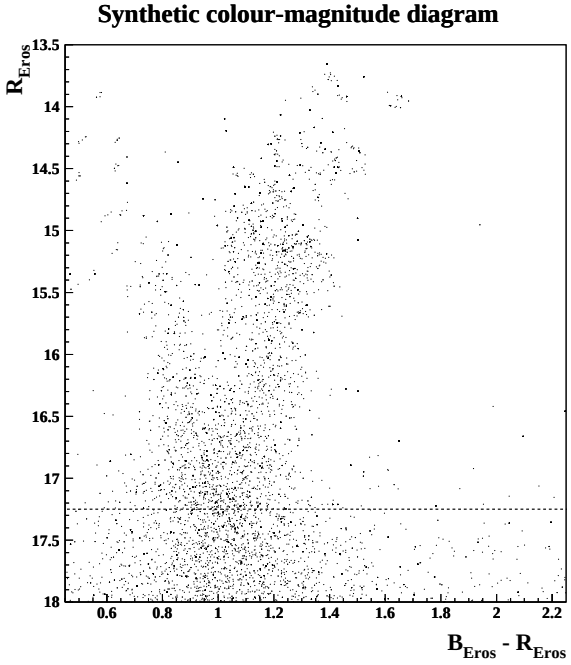

Fig. 9: Artificial colour-magnitude diagram. The dashed line indicates the magnitude cut for the selection of bright stars.

8. Searching the alerts and microlensing events of the MACHO and OGLE collaborations in the EROS data

In view of our low measured optical depth compared to other determinations (see Table 2), it is important to check that microlensing events had not been lost in the analysis procedure in unsuspected ways that are not taken into account by the Monte Carlo detection efficiency calculation. To do this, we looked for Galactic Center events that had been found independently by the MACHO and OGLE collaborations within our observation period in the 15 fields we analyzed, and whose magnitudes are brighter than our cut in the CMD (see §4). We also looked for alerts found by the EROS trigger.

From the MACHO collaboration, we considered the 211 online alerts[3] and 99 published events (Alcock et al. 2000) found by differential photometry. From the OGLE collaboration, we considered the 89 alerts reported during the years 1998 and 1999[4] and the 214 candidates published by Udalski et al. (2000). Regarding the EROS 2 alert system[5], although it was only operational after May 1999, beyond the time period of the data analyzed in this paper, a test version was performed during a limited time yielding three alerts to be considered for the search. From these five sources, a total of 22 events occurred within the observation period considered in this paper (from July 1996 to 31 May 1999) and concerned stars bright enough to pass our magnitude cut.

Of these 22 events, 13 were identified by our analysis pipeline as microlensing candidates, 8 of which have clump-giant sources and an amplification $A_0 > 1.34$. The 9 remaining events were not found. Two were rejected by our selection criteria: one because of excessive fluctuations outside the amplification peak and the other event because the improvement of a microlensing fit over a constant-flux fit was not good enough. Another two events occurred on source-stars that do not appear in the EROS catalog and, as such, cannot be considered for the optical depth measurement. These two stars have a magnitude at the limit of our magnitude cut and are at the edge of brighter stars, which explains their non-appearance in the catalog. Finally, 5 events occured during periods that were at best sparsely sampled by EROS due to bad weather or technical problems. Their non-detection is thus normal and corrected for by our Monte Carlo detection efficiency computation.

Note that the optical depth estimate presented in this paper is unaffected by these results, since none of the "unseen" MACHO and OGLE candidates were not found without a supporting reason (i.e., the analysis pipeline behaved like we expected it to).

9. Discussion and conclusion

The optical depth obtained above (Eq. 10) is low compared to other determinations, as can be seen in Table 2. For direct comparison among these experiments, we also report in this Table the observed optical depths extrapolated to the Baade Window position ($l = 1°, b = -4°$), after applying an optical depth gradient in the l and b directions. We deduced a rough estimate for the gradient: $\partial\tau/\partial b = 0.45 \times 10^{-6} deg^{-1}$ and $\partial\tau/\partial l = 0.06 \times 10^{-6} deg^{-1}$, from several microlensing maps predicted by various non-axisymmetric models (Han & Gould 1995b, Zhao et al. 1996, Bissantz et al. 1997, Evans & Belokurov 2002). The expected opticals depths, for these models, over the interval of Galactic longitude and latitude of our fields ($-6 > b > -2, 6 > l > 0$) ranges roughly from $\tau \sim 1.8 \times 10^{-6}$ to $\tau \sim 0.6 \times 10^{-6}$, as one goes farther away from the Galactic Center. For comparaison with the range of the measured opticals depths in the EROS fields see Fig.7.

The first conclusion that can be drawn is that the quoted measurements are consistent with our optical depth estimate only at the 2σ level. Moreover, the predicted optical depths seem to be more in agreement with our value. Indeed, $\tau_{bulge} \sim 1.3 \times 10^{-6}$ is expected at the Baade Window by Han & Gould (1995b), $\tau_{bulge} \sim 0.8 - 0.9 \times 10^{-6}$ is the inferred estimation by Bissantz et al. (1997) at the same position, and the predicted optical depths by Evans & Belokurov (2002) with two different models are $\tau_{bulge} \sim 1 \times 10^{-6}$ and $\tau_{bulge} \sim 1.5 \times 10^{-6}$, although a third model of these authors gives a higher estimate $\tau_{bulge} \sim 2 \times 10^{-6}$. All of the above mentioned models consider a barred non-axisymmetric bulge. The MACHO and OGLE optical depth measurements are systematically higher than the predicted values, except for the Popowski et al. (2000) determination which is more in agreement with the models. Furthermore, recently Binney, Bissantz & Gerhard (2000) argued that an optical depth for bulge sources as large as the ones inferred by the MACHO collaboration (Alcock et al. 1997, Alcock et al. 2000) is inconsistent with the rotation curve and the local mass-density measurements.

We report 3 microlensing candidates with long durations, $t_{\rm E} > 50$ days: $t_{\rm E} = 56, 108, 146$ days, all in different fields. These events contribute about 30% to the optical depth. Long time scale events, difficult to reconcile with the known mass functions, were already present in the bulge clump-giant sample from Alcock et al. (1997). They found 3 candidates with $t_{\rm E} > 75$ days. It was suggested that they might be due to stellar remnants (Alcock et al. 1997, Han & Gould 1995a) or to directions where there is a spiral arm concentration (Derue et al. 1999, Peale 1999). Popowski et al. (2000) also reported 10 long events, with $t_{\rm E} > 50$ days, contributing 40% to the measured optical depth, half of them being concentrated in one field. In addition, the Einstein ring radius crossing-time distribution of the 214 microlensing candidates found by the OGLE collaboration (Udalski et al. 2000), has the same type of tail toward long time scales ($t_{\rm E} > 50$ days) as the distributions found by MACHO, although they are not concentrated in particular fields but rather uniformly scattered. Recently, Evans & Belokurov (2002) pointed out that bar streaming increases significantly the amplification durations, with a growing gradient in the mean time scales from the near-side to the far-side of the bar.

In our view, the most robust way to resolve the optical depth issue, reconciling Galactic structure with microlensing observations, is to obtain a larger sample of clump-giant events. We expect to increase our sample of candidates by a factor 5 by the time EROS shuts down in 2002. From the preliminary work of Popowski et al. (2000), one may expect the MACHO sample to be increased by

[3] http://darkstar.astro.washington.edu
[4] http://www.astrouw.edu.pl/∼ogle/ogle2/ews/ews.html
[5] http://www-dapnia.cea.fr/Spp/Experiences/EROS/alertes.html

Group	Observed optical depth ($\times 10^{-6}$)	l, b ($^\circ$)	Optical depth Baade Window ($\times 10^{-6}$) $\tau \pm 1\sigma$	No. of events	No. stars ($\times 10^6$)	Bulge seasons
1. EROS 2	$\tau_{bulge} = 0.94^{+0.29}_{-0.30}$	2.5, −4.0	1.08 ± 0.30	16 CG	1.42	~ 3
2. MACHO	$\tau_{bulge} = 3.90^{+1.8}_{-1.2}$	2.6, −3.6	3.86 ± 1.50	13 CG	1.3	190 days
3. MACHO	$\tau = 2.43^{+0.39}_{-0.38}$ $\tau_{bulge} = 3.23^{+0.52}_{-0.50}$	2.7,-3.4	3.11 ± 0.51	99	17	~ 3
4. MACHO	$\tau_{bulge} = 2.0 \pm 0.4$	3.9, −3.8	2.13 ± 0.40	52 CG	2.1	~ 5
5. OGLE	$\tau = 3.30 \pm 1.2$	1, −4	3.3 ± 1.20	12	~ 1	~ 3
6. OGLE II	-	-	-	214	20.5	~ 3

Table 2: Microlensing optical depth estimations at the Baade Window ($l = 1^\circ, b = -4^\circ$), by the EROS 2, MACHO and OGLE collaborations : 1. this paper, 2. Alcock et al. 1997, 3. Alcock et al. 2000, 4. Popowski et al. 2000, 5. Udalski et al. 1994b, 6. Udalski et al. 2000.

a factor 1.3. Moreover, the OGLE data set represents a potentially rich source of additional events. In the future, the coming of new survey telescopes such as VST and VISTA, will enhance the possibility to distinguish between Galactic models, especially if microlensing observations are done in the K band in the inner $5^\circ \times 5^\circ$ region of the Galactic Center (Gould 1995a, Evans & Belokurov 2002). Thus, the prospects for clarifying this question over the next few years are very promising.

Acknowledgements. We are grateful to D. Lacroix and the technical staff at the Observatoire de Haute Provence and A. Baranne for their help in refurbishing the MARLY telescope and remounting it in La Silla. We are also grateful to the technical staff of ESO, La Silla for the support given to the EROS project. We thank J-F. Lecointe and A. Gomes for the assistance with the online computing. Work by A. Gould was supported by NSF grant AST 02-01266 and by a grant from Le Centre Français pour L'Accueil et Les Échanges Internationaux. Work by C. Afonso was supported by PRAXIS XXI fellowship-FCT/Portugal.

References

Afonso C., Alard C., Albert J.-N., et al. (EROS collaboration) 1999, A&A, 344, L63
Alcock C., Allsman R. A., Alves D. R., et al. (MACHO collaboration) 1997, ApJ, 479, 119
Alcock C., Allsman R. A., Alves D. R., et al. (MACHO collaboration) 2000, ApJ, 541, 734
Ansari, R. (EROS collaboration) 1996, Vistas in Astronomy, 40, 519
Bahcall J.N. & Soneira R.M. 1980, ApJS, 44, 73
Bauer F. et al. (EROS collaboration) 1997, Proceeding of the "Optical Detectors for Astronomy" workshop, ESO
Binney J., Gerhard O. E., Stark A. A., et al. 1991, MNRAS, 252, 210
Binney J., Bissantz N. & Gerhard O. 2000, ApJLetters, 537, L99
Bissantz N., Englmaier P., Binney J., Gerhard O. 1997, MNRAS, 289, 651
Derue F., Afonso C., Alard C., et al. (EROS collaboration) 1999, A&A, 351, 87
Derue F., Afonso C., Alard C., et al. (EROS collaboration) 2001, A&A, 373, 126
Dwek E., Arendt R. G., Hauser M. G., et al. 1995, ApJ, 445, 716
Evans, N.W. & Belokurov, V. 2002, astro-ph/0202042
Goldman B., Afonso C., Alard C., et al. (EROS collaboration) 2002, A&A, 389, L69
Gould A. 1992, ApJ, 392, 442
Gould A. 1994, ApJLetters, submitted, (astro-ph/940860)
Gould A. 1995a, ApJ, 446, L71
Gould A. 1995b, ApJ, 447, 491
Griest K. 1991, ApJ, 366, 412
Han C. & Gould A. 1995a, ApJ, 447, 53
Han C. & Gould A. 1995b, ApJ, 449, 521
Hardin D., Afonso C., Alard C., et al. (EROS collaboration) 2000, A&A, 362, 419
Holtzman J. A., Watson A. M., Baum W. A., et al. 1998, AJ, 115, 1946
Kiraga M. & Paczyński B. 1994, ApJ, 430, L101-L104
Kuijken K. 1997, ApJ, 486, L19
Lasserre T., Afonso C., Albert J.-N., et al. (EROS collaboration) 2000, A&A, 355, L39
Nikolaev S. & Weinberg M. D. 1997, ApJ, 487, 885
Paczyński B. 1986, ApJ, 304, 1
Paczyński B. 1991, ApJ, 371, L63-L67
Paczyński B., Udalski A. Szymanski M., et al. 1999, Act. Astr., 49, 319
Palanque-Delabrouille N. (EROS collaboration) 1997, PhD thesis: Research on Galactic Dark Matter implied by Gravitatinal Lensing, Université de Paris 7 and University of Chicago
Peale S. J. 1999, ApJ, 524, L67
Popowski P., Cook K. H., Drake A. J., et al. (MACHO collaboration) 2000, In Menzias J.W., Sackett P.D. eds, Proc. Microlensing 2000, ASP Conference Series, in press (astro-ph/005466)
Stanek K. Z., Paczynski B., Udalski A., et al. (OGLE collaboration) 1995, AAS, 186, 304
Udalski A., Szymanski M., Kaluzny J.,et al. (OGLE collaboration) 1994a, ApJ, 426, L69
Udalski A., Szymanski M., Stanek K. Z., et al. (OGLE collaboration) 1994b, Act. Astr., 44, 165
Udalski A., Zebrun K., Szymanski M., et al. (OGLE collaboration) 2000, Act. Astr., 50, 1
Wozniak P. R., Udalski A., Szymanski M. et al. (OGLE collaboration) 2001, Act. Astr., 51, 175

Zhao H., Rich R. M. & Spergel D. N. 1996, MNRAS, 282, 175
Zhao H. & Mao S. 1996, MNRAS, 283, 1197

	EROS 2 candidates	α (J2000)	δ (J2000)	$R_{\rm EROS}$	$B_{\rm EROS}$	t_0	$t_{\rm E}$	A_0	χ^2/d.o.f.
#1	EROS-BLG-16	18:04:57.5	-29:40:9.8	16.1	17.3	2714.62±0.12	4.64±0.24	1.77	199/551
#2	EROS-BLG-35	18:13:26.7	-27:21:53.9	16.2	17.3	3017.83±0.29	8.46±0.31	1.91	216/261
#3	EROS-BLG-3	18:00:46.4	-29:06:55.7	16.3	17.9	3004.18±0.28	9.30±0.47	1.77	295/541
#4	EROS-BLG-28	18:08:51.3	-28:27:11	16.2	17.6	2631.01±0.06	10.04±0.12	2.63	862/460
	MACHO 97-BLG-05								
#5	EROS-BLG-2	18:01:02.5	-29:00:11.6	15.1	16.6	3382.99±0.33	10.38±0.35	1.61	1169/518
	OGLE 1999-BUL-06								
#6	EROS-BLG-32	18:11:51.5	-29:00:33.5	16.5	17.5	3034.41±0.26	10.84±0.48	1.87	197/486
#7	EROS-BLG-13	18:04:33.6	-28:07:32.2	15.1	16.4	3105.74±0.20	13.05±0.35	1.60	313/465
	EROS-98-BLG-4								
	OGLE 1998-BUL-23								
#8	EROS-BLG-33	18:14:32.5	-29:14:46.4	15.7	16.7	2646.50±0.26	15.69±0.26	1.60	911/448
#9	EROS-BLG-31	18:12:43.4	-29:38:28.5	16.4	17.5	2812.56±0.03	18.29±0.18	5.84	1681/208
	with blending	$C_{\rm R}$	$C_{\rm B}$						
		0.62±0.05	1.00±0.08	16.9	17.6	2812.59±0.04	22.31±1.78	8.04	406/198
#10	EROS-BLG-23	18:07:06.4	-28:42:32.8	16.3	17.5	3071.07±0.39	20.63±0.39	2.58	255/522
	EROS-98-BLG-2								
#11	EROS-BLG-11	18:04:9.7	-27:44:35	15.8	17.2	2790.94±0.19	30.25±0.38	1.98	883/552
	OGLE BUL_SC35-144974								
	MACHO 97-BLG-58								
	with blending	$C_{\rm R}$	$C_{\rm B}$						
		0.73±0.14	0.55±0.11	16.2	17.8	2791.00±0.20	35.46±3.25	2.49	715/550
#12	EROS-BLG-5	18:01:10.2	-29:48:55	16.1	17.5	3423.02±0.18	35.57±0.35	2.17	576/749
	OGLE 1999-BUL-07								
	MACHO 99-BLG-12								
#13	EROS-BLG-18	18:06:20.4	-27:56:13	16.3	17.4	2987.59±0.41	35.83±0.86	2.90	554/454
#14	EROS-BLG-4	18:00:6.9	-29:38:06	16.7	18.5	2743.93±0.08	62.89±0.32	7.88	422/774
	MACHO 97-BLG-26								
#15	EROS-BLG-29	18:10:56.2	-29:24:24.4	14.3	15.5	3363.14±0.27	116.31±0.79	3.82	938/551
	with parallax	ϕ	$\pi_{\rm E}$						
		-1.492±0.567	0.229±0.023	14.3	15.5	3362.90±0.75	108.34±0.68	24.40	537/549
#16	EROS-BLG-12	18:03:53.2	-27:57:36	15.8	17.2	2491.63±0.37	109.50±0.75	5.93	1484/452
	MACHO 96-BLG-12								
	with parallax	ϕ	$\pi_{\rm E}$						
		-0.138±0.22	0.272±0.063	15.8	17.2	2472.50±0.94	145.61±2.72	8.81	552/438

Table 3: The list of the 16 EROS 2 microlensing candidates (with clump-giant sources and $u_0 < 1$). The first column indicates the number and name of the EROS 2 candidate. The corresponding MACHO and OGLE candidates/alerts are shown below the EROS event name, as well as the EROS alerts, when these have been reported. The following two columns (2 and 3) refer to the sky coordinates of the source star. The next columns (4 and 5) show the $R_{\rm EROS}$ and $B_{\rm EROS}$ magnitudes of the source stars. Columns number 6 and 7 refer to the date of maximum amplification t_0 and the time scale $t_{\rm E}$ of the candidate. The last two columns (8 and 9) indicate the maximum amplification A_0 of the light curve and the reduced χ^2 of the microlensing fit. For candidates #9 and #11, the results of the microlensing fit taking blending into account are shown. The parameters $C_{\rm R}$ and $C_{\rm B}$ refer to the blending coefficients for the red and blue light curve (see §3 for blending definiton). Candidates #15 and #16 are parallax events, the parameters $\pi_{\rm E}$ and ϕ being respectively the amplitude of the displacement in the Einstein ring due to the Earth's orbital motion and the phase of the displacement.

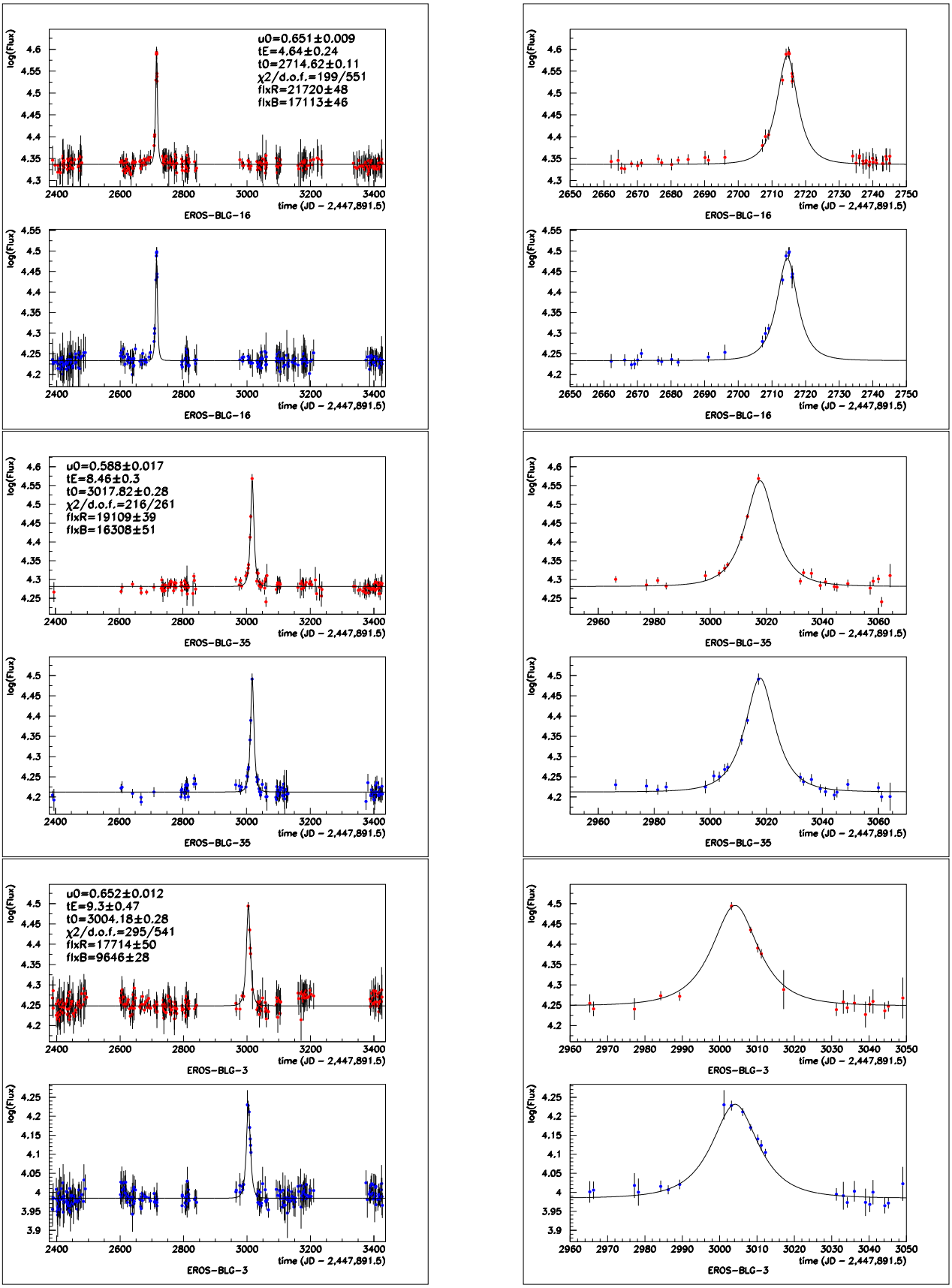

Fig. 10: The light curves of the EROS 2 microlensing candidates #1 to #3 (see Table 3). In each box the upper light curve refers to the EROS red filter and the lower light curve to the EROS blue filter. Full span of the light curves is shown in the left column and corresponding zoomed light curves are in the right column. The 5 parameters obtained by the fit of the Paczyński profile are shown (on full span only), as well as the χ^2 values of the fit.

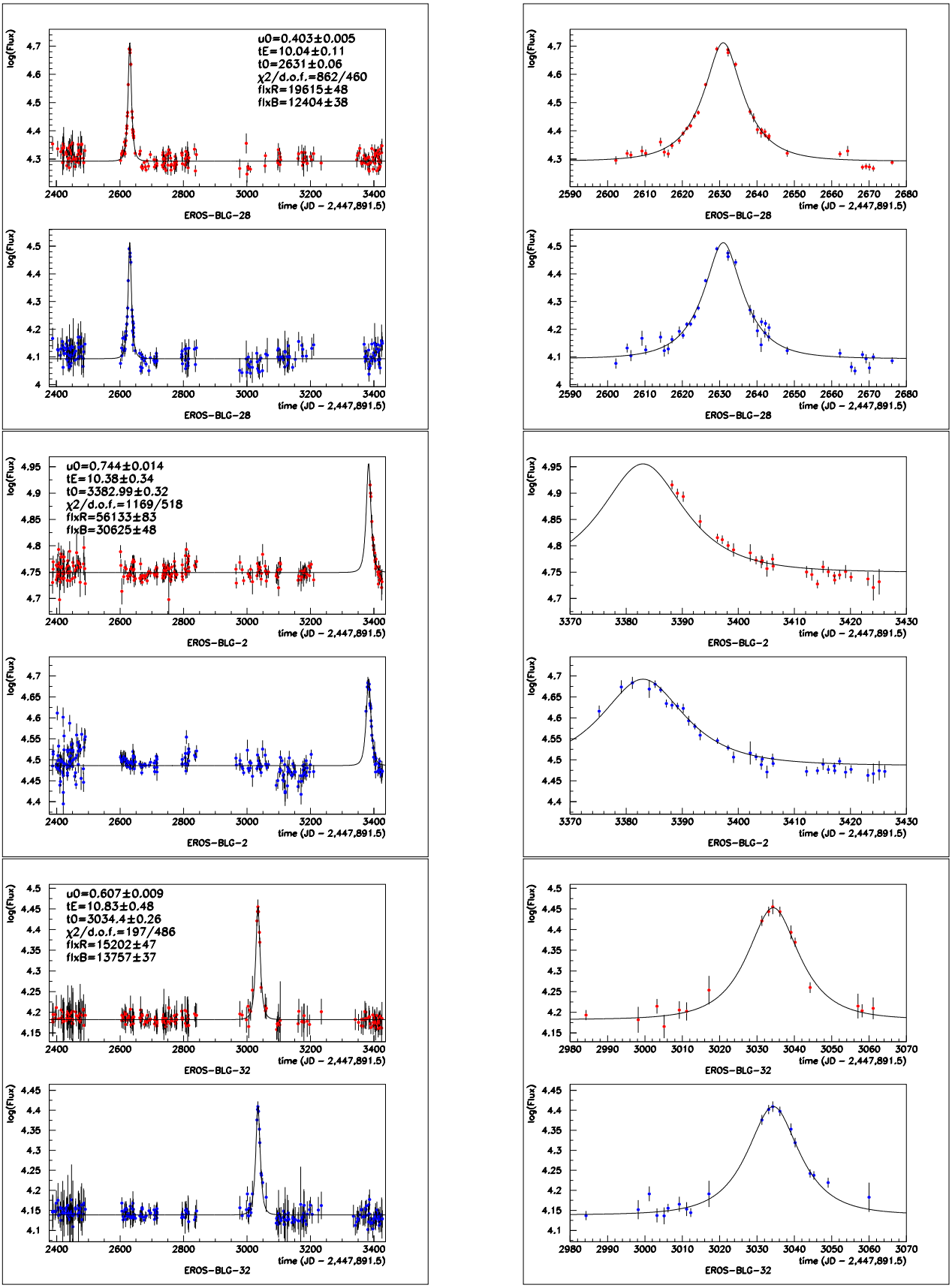

Fig. 11: The light curves of the EROS 2 microlensing candidates #4 to #6 (see Table 3). In each box the upper light curve refers to the EROS red filter and the lower light curve to the EROS blue filter. Full span of the light curves is shown in the left column and corresponding zoomed light curves are in the right column. The 5 parameters obtained by the fit of the Paczyński profile are shown (on full span only), as well as the χ^2 values of the fit.

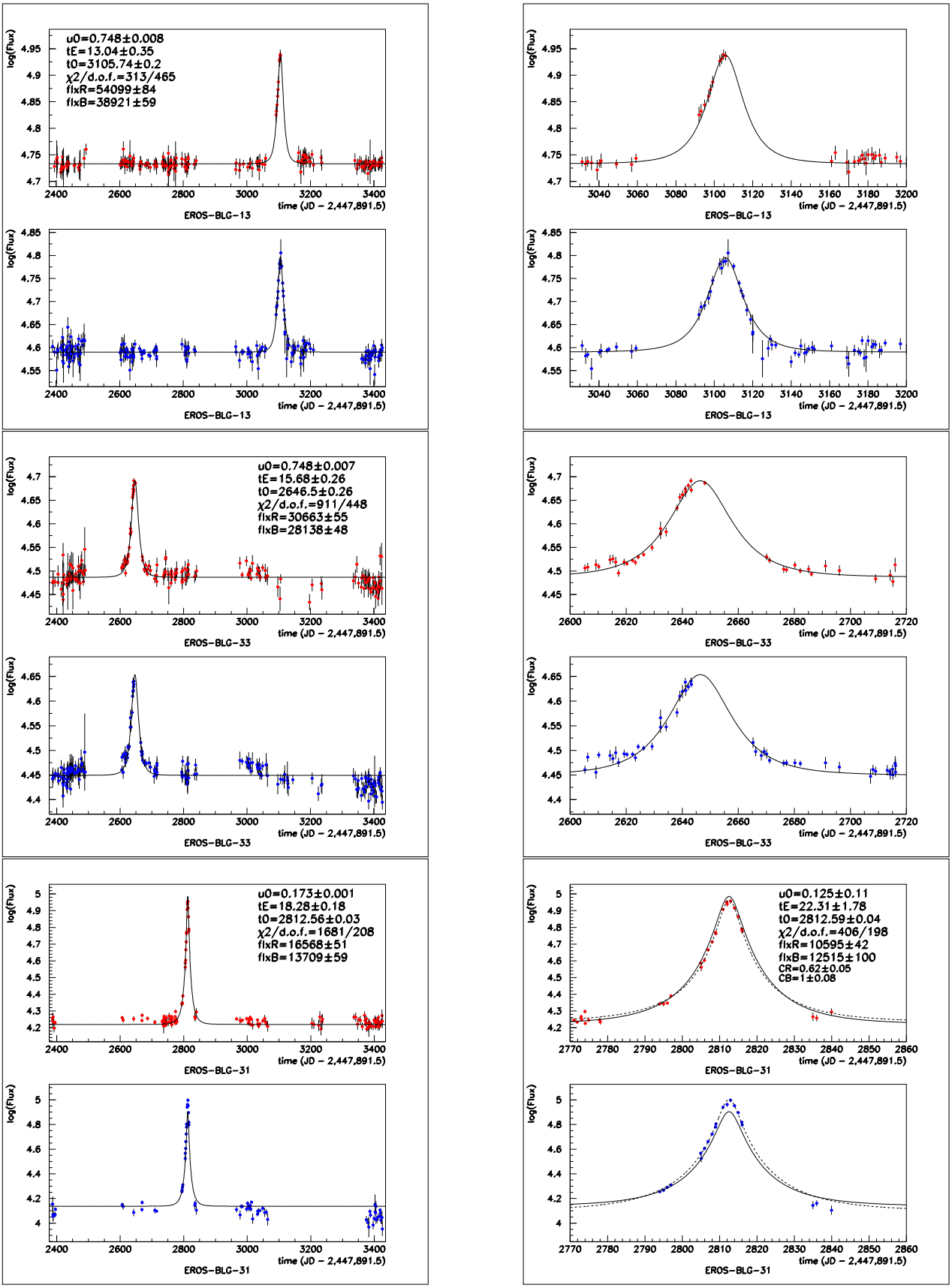

Fig. 12: The light curves of the EROS 2 microlensing candidates #7 to #9 (see Table 3). In each box the upper light curve refers to the EROS red filter and the lower light curve to the EROS blue filter. Full span of the light curves is shown in the left column and corresponding zoomed light curves are in the right column. The 5 parameters obtained by the fit of the Paczyński profile are shown (on full span only), as well as the χ^2 values of the fit. For candidate #9 the dashed line refers to the fit when blending is taken into account. The left light curves of this candidate indicate the parameters of the microlensing fit without blending and the zoom (right light curve) shows the parameters of the fit with blending.

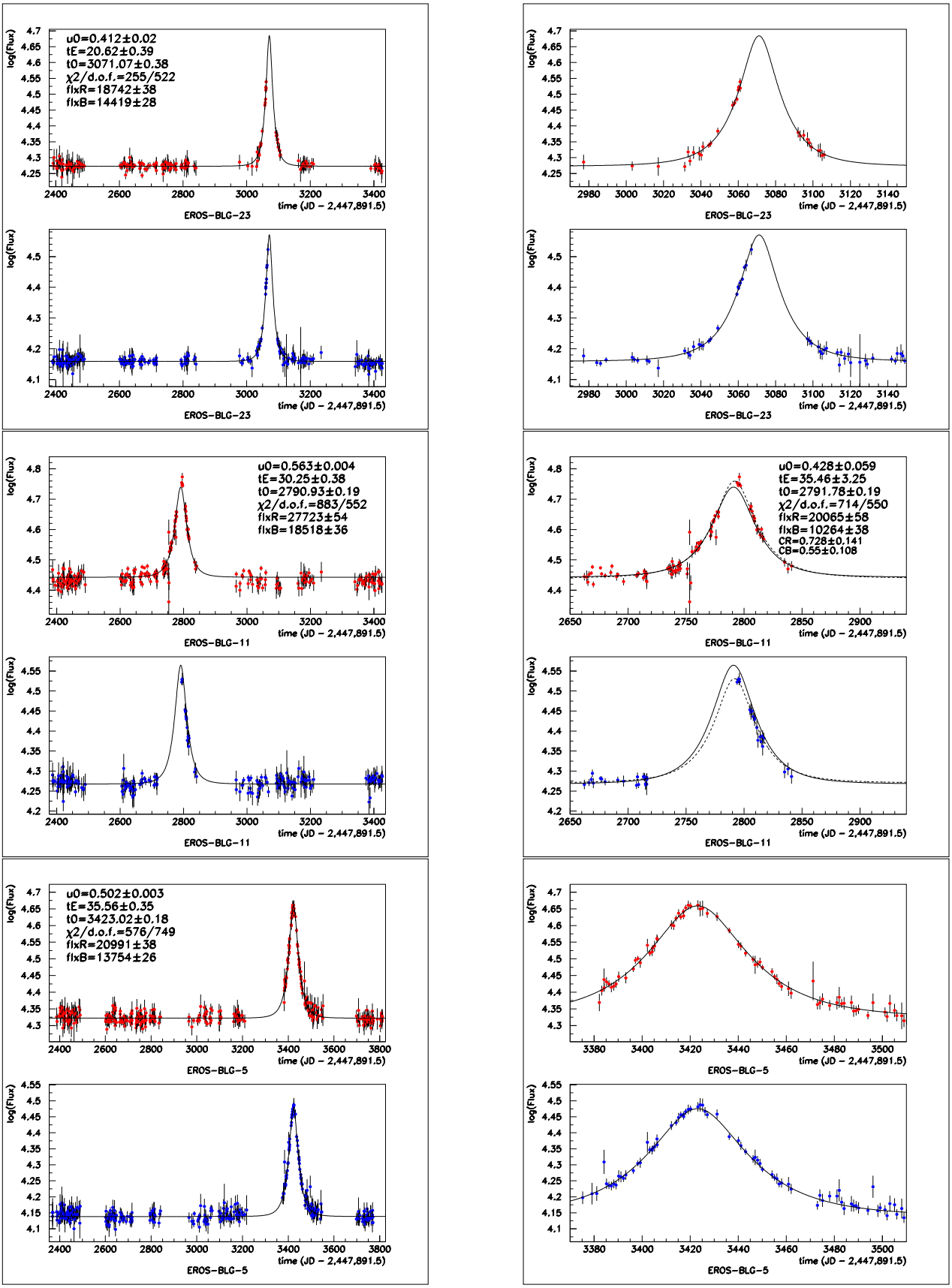

Fig. 13: The light curves of the EROS 2 microlensing candidates #10 to #12 (see Table 3). In each box the upper light curve refers to the EROS red filter and the lower light curve to the EROS blue filter. Full span of the light curves is shown in the left column and corresponding zoomed light curves are in the right column. The 5 parameters obtained by the fit of the Paczyński profile are shown (on full span), as well as the χ^2 values of the fit. For candidate #11 the dashed line refers to the fit when blending is taken into account. The left light curves of this candidate indicate the parameters of the microlensing fit without blending and the zoom (right light curve) shows the parameters of the fit with blending.

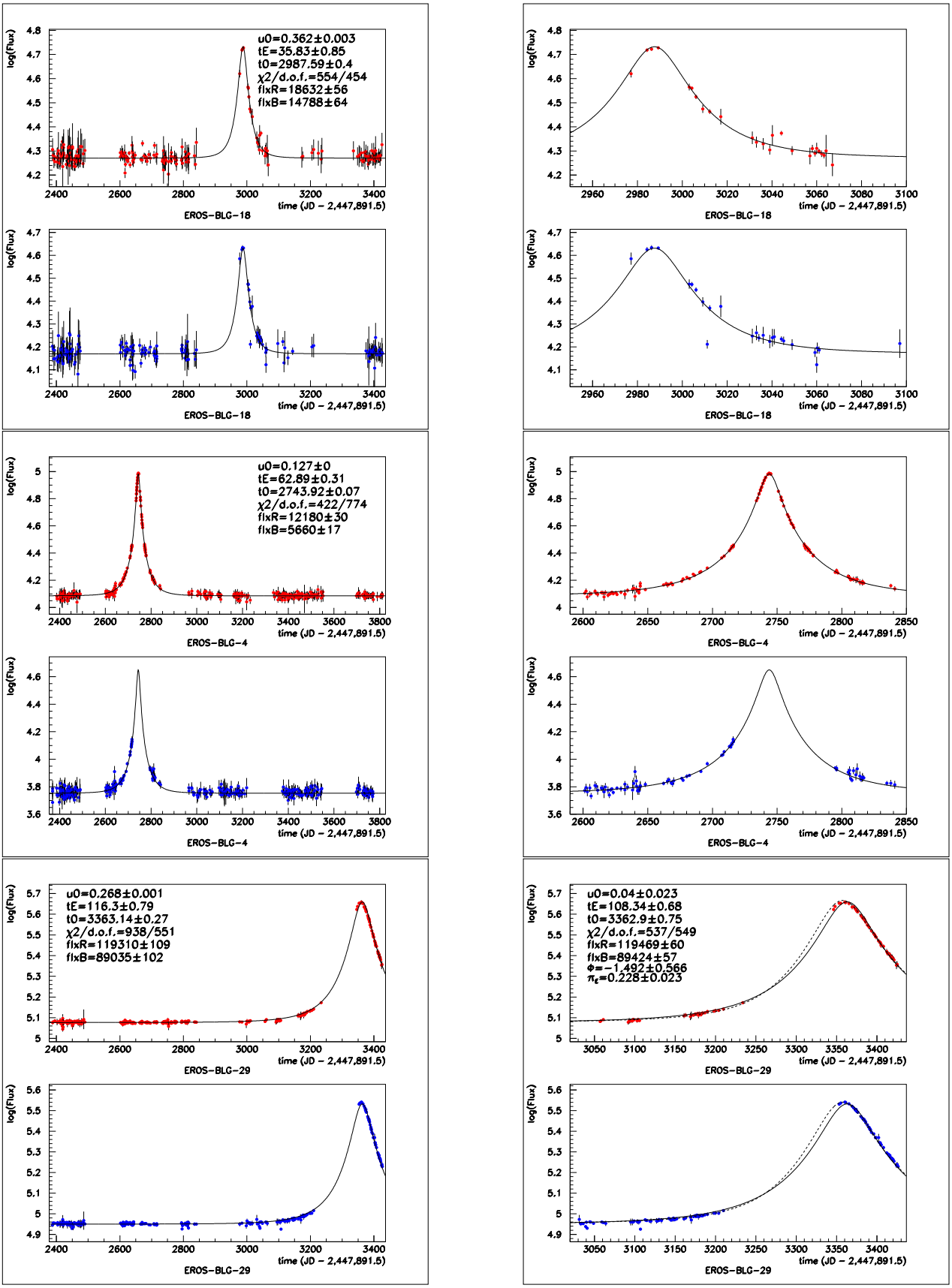

Fig. 14: The light curves of the EROS 2 microlensing candidates #13 to #15 (see Table 3). In each box the upper light curve refers to the EROS red filter and the lower light curve to the EROS blue filter. Full span of the light curves is shown in the left column and corresponding zoomed light curves are in the right column. The 5 parameters obtained by the fit of the Paczyński profile are shown (on full span), as well as the χ^2 values of the fit. For candidate #15 the dashed line refers to the fit when parallax is taken into account. The left light curves of this candidate indicate the parameters of the microlensing fit without parallax and the zoom (right light curves) shows the parameters of the fit with parallax.

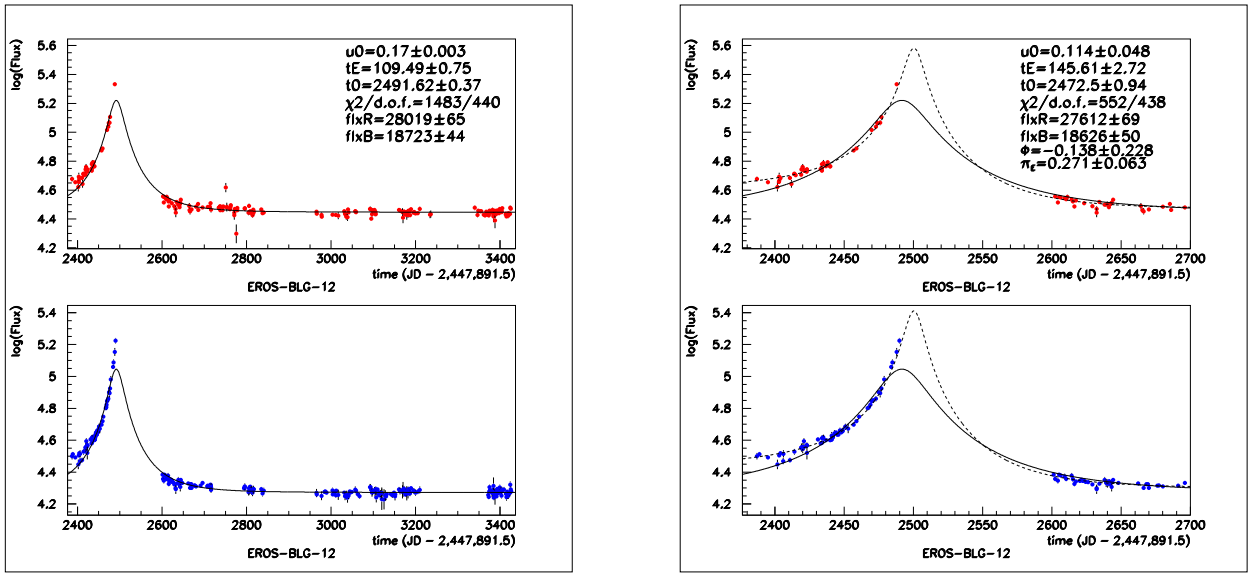

Fig. 15: The light curves of the EROS 2 microlensing candidate #16 (see Table 3). In each box the upper light curve refers to the EROS red filter and the lower light curve to the EROS blue filter. Full span of the light curves is shown in the left column and corresponding zoomed light curves are in the right column. The 5 parameters obtained by the fit of the Paczyński profile are shown (on full span), as well as the χ^2 values of the fit. For candidate #16 the dashed line refers to the fit when parallax is taken into account. The left light curves of this candidate indicate the parameters of the microlensing fit without parallax and the zoom (right light curves) shows the parameters of the fit with parallax.